MITSUBISHI ELECTRIC RESEARCH LABORATORIES
https://www.merl.com

Spectrally sparse optical coherence tomography

Atalar, Okan; Millar, David S.; Wang, Pu; Koike-Akino, Toshiaki; Kojima, Keisuke; Orlik, Philip V.; Parsons, Kieran

TR2020-156 December 11, 2020

Abstract

Swept-source optical coherence tomography (OCT) typically relies on expensive and complex swept-source lasers, the cost of which currently limits the suitability of OCT for new applications. In this work, we demonstrate spectrally sparse OCT utilizing randomly spaced low-bandwidth optical chirps, suitable for low-cost implementation with telecommunications grade devices. Micron scale distance estimation accuracy with a resolution of 40 Um at a standoff imaging distance greater than 10 cm is demonstrated using a stepped chirp approach with approximately 23% occupancy of 4 THz bandwidth. For imaging of sparse scenes, comparable performance to full bandwidth occupancy is verified for metallic targets.

Optics Express

Mitsubishi Electric Research Laboratories, Inc.
201 Broadway, Cambridge, Massachusetts 02139

Spectrally sparse optical coherence tomography

Okan Atalar,[1,2] David S. Millar, [2*] Pu Wang, [2]
Toshiaki Koike-Akino, [2] Keisuke Kojima, [2]
Phillip V. Orlik, [2] Kieran Parsons, [2]

[1] *Department of Electrical Engineering, Stanford University, Stanford, CA 94305, USA*
[2] *Mitsubishi Electric Research Laboratories (MERL), 201 Broadway, Cambridge, MA 02139, USA*
[*] *Corresponding author: millar@merl.com*

Abstract: Swept-source optical coherence tomography (OCT) typically relies on expensive and complex swept-source lasers, the cost of which currently limits the suitability of OCT for new applications. In this work, we demonstrate spectrally sparse OCT utilizing randomly spaced low-bandwidth optical chirps, suitable for low-cost implementation with telecommunications grade devices. Micron scale distance estimation accuracy with a resolution of 40 μm at a standoff imaging distance greater than 10 cm is demonstrated using a stepped chirp approach with approximately 23% occupancy of 4 THz bandwidth. For imaging of sparse scenes, comparable performance to full bandwidth occupancy is verified for metallic targets.

1. Introduction

Optical coherence tomography (OCT) is a widely used imaging technology with micrometer scale axial resolution [1–4], and has found applications in areas such as medical imaging [5–7], nondestructive testing [8, 9], and environmental three-dimensional (3D) mapping [10–12]. OCT systems were initially designed with a semi-coherent source and a moving mirror to physically change the optical path length in the reference arm of the interferometer [13]. Spectral domain OCT systems use a spectrometer detector, which limits the accuracy and speed problems related to mechanical tuning [14]. Swept-source OCT systems use a frequency swept optical source, such as a swept-source laser [15–17]. This architecture enables the use of a single point detector and an interferometer with no moving parts, and has therefore become the preferred architecture for high performance OCT systems since it offers significantly higher signal-to-noise ratio (SNR) [18–20].

Despite the significant advances in OCT systems, the high cost of swept-source OCT currently limits the scope of its application. The high cost of such systems is, in significant part, due to the cost and complexity of a laser which is able to achieve linear frequency sweeping in time, over a range of 10 THz or more [21], often achieved with high-speed mechanically tuned cavities [22–26], or high-speed electro-optic tuning [27]. The cost and complexity of such devices may be broadly attributed to the difficulties associated with micro opto-mechanical assembly in the case of mechanically tuned cavities or high-speed electro-optic based swept-source lasers. While these difficulties do not prevent the manufacture of high precision devices, they are a significant impediment for the reduction in total system cost, and the use of OCT for novel applications. We note that the cost of commercially available spectral domain OCT systems are on the order of tens of thousands of US dollars [28], while swept-source OCT systems are considerably more expensive.

However, we note that applications for which targets are spatially sparse (such as non-destructive testing, profilometry, coating thickness measurement, etc.) [29, 30] the expected target spectrum may be considered as a mixture of a small number of sinusoids, which may be recovered when sampled with spectrally sparse illumination. A well developed sparse sensing strategy in radar is uniformly spaced stepped chirp [31, 32], which exhibits a trade-off between range and axial resolution, where resolution is defined as the ability to resolve two or more closely spaced targets.

However, since many applications require tens of centimeters range and micron scale resolution, the occupied bandwidth needs to be high for uniformly spaced stepped chirp approach. High resolution ranging using an optical frequency comb has been demonstrated in [33], but the unambiguous imaging range is limited by the comb spacing. Ranging using a single laser with low bandwidth (BW) frequency sweeps (GHz range) has also been demonstrated, e.g., in [34, 35]. Even though a single low BW chirp allows a single target to be imaged with high ranging accuracy, the requirement of long maximum range and micron scale resolution necessitates covering a high BW to avoid ambiguities during scanning the sample (since the beam cannot remain small throughout the imaging range, it may overlap with multiple reflectors at different heights). To overcome this limitation, a random stepped approach can be used [36, 37].

One method by which this may be implemented is to use a set of discrete lasers to provide a large optical bandwidth, an optical switch to multiplex them, and a phase modulator such as a Mach–Zehnder in-phase/quadrature (I/Q) modulator to provide chirp when driven with an appropriate radio frequency (RF) signal. The advantages of such a configuration are three-fold; i) the relatively low cost of such components (which are commonly used in telecommunications systems); ii) the potential for further cost reduction by integration onto a photonic integrated circuit; and iii) the improvement in linearity that is achievable with a chirp of several tens of GHz [38], that is generated in the RF domain. The reconstruction fidelity of such systems is related to sparsity of targets and total illumination BW. Tunable lasers with high BW usually suffer from nonlinearities when trying to achieve a linear chirp, degrading image reconstruction [39].

In this paper, we demonstrate an illumination strategy for imaging sparse targets. We propose a novel optical architecture that makes use of telecommunications grade devices, therefore offering low-cost and scalability, and achieves high-performance imaging of sparse targets. Mach-Zehnder I/Q modulators offer the speed and efficiency necessary for implementing the proposed approach [35, 40], while the proposed method will continue to scale favorably, as modulator bandwidth and performance will increase with the requirements of the telecommunications industry.

We demonstrate random stepped chirp OCT using an all-fiber common path interferometer by covering a part of the BW, and show good performance results comparable to full chirp when imaging metallic targets. Using the proposed illumination technique, we derive estimates on the probability of error for sensing sparse targets. In particular, we demonstrate that random stepped chirp with 23% occupancy of 4 THz bandwidth for imaging metallic targets can achieve comparable performance with full chirp sweep. This facilitates developing low-cost and scalable OCT systems that can be used for a wide range of imaging applications.

2. Random sparse chirp OCT

Distance of targets can be estimated by linearly chirping the frequency of a light source, and interfering the returned light after reflecting from the target with itself. The distance of the target is proportional to the beat frequency due to interference of the two beams.

Linear chirp image domain is usually achieved through taking the fast Fourier transform (FFT) of the time-signal, and then taking the magnitude. The covered BW is inversely proportional to the attainable resolution, and using Abbe resolution criterion, this can be quantified as $c/(2BW)$, where c is the speed of light in air, and BW is the covered bandwidth through the chirp. It should be noted that although a low BW chirp can be used for ranging through matched-filtering, this approach does not allow two or more closely spaced targets to be imaged simultaneously.

To retain the spatial resolution, while reducing the scanned BW, linear stepped chirp approach can be used, where a constant frequency difference is used between chirps, and each low-resolution image reconstructed through an FFT. This approach is analogous to linear stepped chirp radar, and is well known in the radar literature [31, 32]. The time-signal captured for each low BW

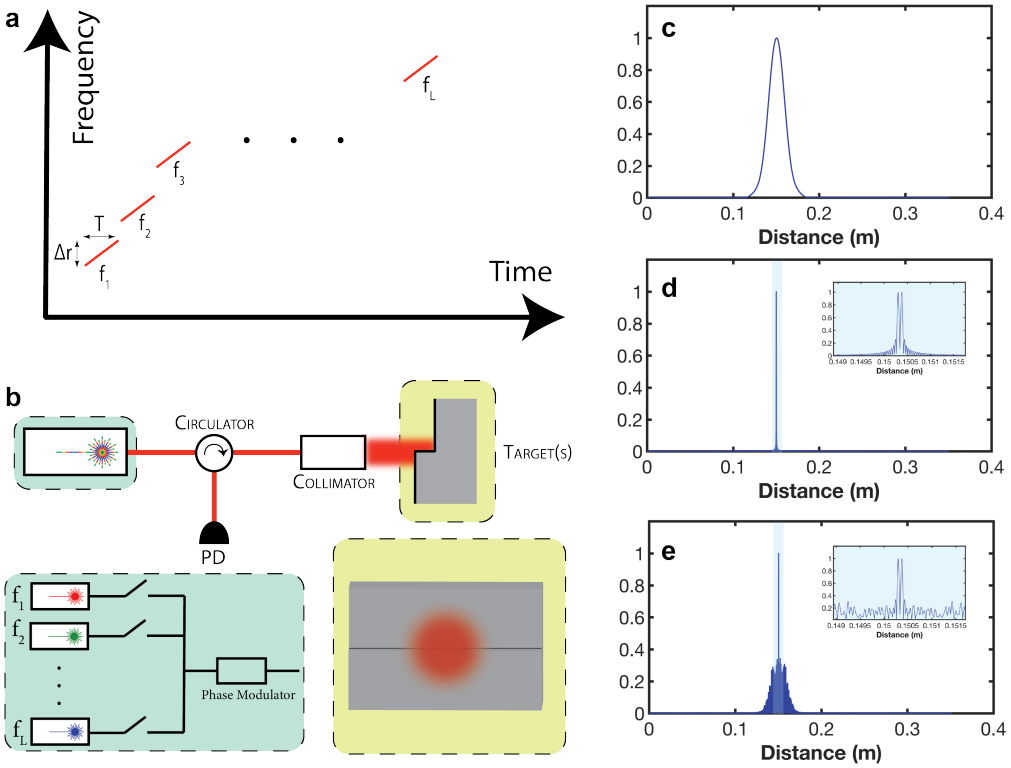

Fig. 1. Stepped chirp OCT System. **(a)** Stepped chirp OCT time-frequency plot with center frequencies for chirps $f_1, f_2, f_3, \ldots, f_L$, chirp duration T, and chirp bandwidth Δr. **(b)** The imaging system consists of a stepped chirp light source, circulator, partially reflective (providing the common path reference signal) collimator to illuminate target(s), and a photodetector (PD). The stepped chirp light source could be realized by connecting multiple single frequency lasers and multiplexing with a phase modulator. **(c)** Two targets placed at 15 cm (with a separation of 75 μm) from the imaging system reconstructed using the magnitude of the Fourier transform of the received waveform. Imaging parameters: 15 GHz chirp bandwidth, detector sampling rate of 400 MHz, chirp rate of 7.3026×10^{16} Hz/s. **(d)** Same imaging parameters as in **c** with same reconstruction technique, except the covered bandwidth is 3.74 THz. **(e)** Stepped chirp imaging with same small bandwidth as in **c** (i.e., 15 GHz), 63 frequencies used with matched-filtering for image reconstruction, covering around 25% of bandwidth compared to part **d**.

chirp at the receiver is written as follows:

$$I_i(t) = \mathrm{DC} + \sum_{a=1}^{N} R_a \cos\left(\frac{4\pi f_i D_a}{c} + \frac{4\pi}{c}\left(\frac{-\Delta r}{2} + \frac{\Delta r t}{T}\right) D_a\right) + n(t),$$
$$i \in \{1, 2, \ldots, L\}, \qquad t \in [0, T), \tag{1}$$

where L is the total number of low BW chirps, f_i is the center frequency for the i^{th} chirp, N the number of targets illuminated by imaging beam, D_a the distance of the targets to the receiver, R_a the reflectivity of the targets, T the duration of each low BW chirp, Δr the bandwidth covered by each chirp, $n(t)$ additive white Gaussian noise (AWGN), and DC the constant intensity term. The high-resolution image is then obtained by multiplying each with the right phase, summing

these terms, and taking the magnitude; equivalent to matched-filtering. The problem with linear stepped chirp approach is that the unambiguous imaging range is now limited by the spacing between the chirps, $c/(2\Delta f)$, where Δf is the linear spacing between chirps, so that to achieve high resolution while also keeping low occupancy BW, the unambiguous range needs to be small, making it unconventional for many applications.

Random spacing between chirps can also be used. In this case, the reconstruction method is identical to linear stepped chirp, as expressed in

$$\hat{I}(d) = \left| \sum_{i=1}^{L} \tilde{I}_i\Big(\frac{2ds}{c}\Big) \exp\Big(-\jmath \frac{4\pi f_i d}{c}\Big) \right|, \tag{2}$$

where $\tilde{I}_i(f)$ is the Fourier transform of $I_i(t)$ ($\jmath$ denotes the imaginary unit). The advantage of this method is that the unambiguous range is now only limited by the sampling rate of the detector by $cf_s/(4s)$, where f_s is the sampling rate of detector, $s = \Delta r/T$ is the chirp rate, and $d \in [0, cf_s/(4s))$ is the reconstruction distance. Unambiguous imaging range of $c/(2\Delta f)$ is valid for the linear stepped chirp approach if $cT/2 > c/(2\Delta f)$, and unambiguous imaging range of $cf_s/(4s)$ is valid for the random stepped chirp approach if $cT/2 > cf_s/(4s)$. The unambiguous imaging range is always upper bounded by $cT/2$ because the reflected chirp signal from the target needs to return back to the detector before the chirp duration is over. This condition, however, is usually met for most chirping situations, and thus the linear stepped chirp approach and random stepped chirp approach usually have unambiguous ranges of $c/(2\Delta f)$ and $cf_s/(4s)$, respectively. The random stepped chirp approach therefore avoids the trade-off between unambiguous range and resolution present in linear stepped chirp approach, and the unambiguous range could be increased by sampling faster with the detector. The main limitation of this approach, also encountered in sparse radar imaging, is relatively high side lobes. The smaller the occupation bandwidth, the larger the side lobes, and this makes it more difficult to understand the image domain, since side lobes appear like targets [36, 37, 41].

The proposed sparse chirp OCT imaging system is shown in Fig. 1(a): Small linear chirps, randomly spaced, are used for illumination of the target(s). One possible architecture for realizing the system is shown in Fig. 1(b), where a stepped chirped source is physically realized by connecting discrete single frequency lasers, and having switches with a phase modulator. This approach will allow two (or more) targets illuminated simultaneously to be reconstructed. The reconstruction of two targets spaced by 75 μm, and placed at a distance of 15 cm from the receiver is shown in Fig. 1(c)–(e) using a single low BW chirp, high BW chirp, and random sparse chirp occupying 25%, respectively. It is clear from the plots that the random sparse chirp and full chirp are able to identify the two closely spaced targets, whereas the single chirp is unable to detect the single target. It is also seen that side lobes appear in the random sparse chirp method. This will be an issue especially if the number of closely spaced targets is not small (breaking the sparsity assumption).

To estimate the number and location of targets, we used matched-filtering in (2), followed by thresholding based on the peak. As sparse reconstruction methods are well-known in the radar literature, there are various alternative methods for reconstruction that exploit the sparsity of the signal [42]. Compressed sensing has been used to reduce the amount of data acquisition required for OCT volumetric image reconstruction. Specifically, compressed sensing approach to reduce the number of scanned points for volumetric image reconstruction has been demonstrated in [43], and compressed sensing approach in both scanning pattern and spectral measurements for volumetric image reconstruction has been demonstrated in [44]. The reason why we focused on matched-filtering followed by thresholding based on the peak is because this approach allows simple closed-form solutions to be derived for expected performance given the imaging parameters.

We present a basic probabilistic framework to estimate the probability of error for misdetection

given a sparse scene using our proposed architecture and algorithm. An error is assumed to occur if the number of estimated targets is incorrect, or the estimated locations are incorrect. To capture imperfection of the laser sources, we assume that each laser frequency has a normal distribution for its center frequency, and this allows us to test the reconstruction robustness. Knowing the occupancy bandwidth and the standard deviation of the center frequencies, we can derive the error probability for misdetection. In particular, the goal is to localize the correct number of targets and their respective locations.

To estimate the error probability, we need to compare the distribution of the peak(s) to the maximum side lobe, since peak based thresholding is used. In other words, an error would occur if at least one of the side lobes (i.e. the maximum side lobe) exceeds a threshold. For simplicity, we assume that the reflectivity for all the different targets with different height profiles are the same (peaks have identical distributions).

If the number of stepped chirps, L, used during reconstruction is sufficiently large, then the side lobes can be approximated as circularly symmetric complex Gaussian distributions using the Central Limit Theorem (CLT), where the real and imaginary parts are identically and independently distributed as $\mathcal{N}(0, \frac{1}{2L})$ (when normalized to the peak). Since we are taking the magnitude for reconstruction as in (2), the cumulative distribution function (CDF) for the maximum side lobe follows a Rayleigh distribution [45]. Each peak (corresponding to a target) has a sinc function profile due to the rectangular windowing applied during the FFT. The CDF for the maximum side lobe is equivalent to the maximum of independent Rayleigh distributions scaled by a sinc function. This scaling is captured by σ_u^2 for the different Rayleigh distributions. To ensure that the independence assumption is valid between the scaled Rayleigh distributions, the parameter P is used, which is a function of the covered BW of the chirp (a tuning parameter to ensure independence between Rayleigh distributions). The CDF for the maximum side lobe can be expressed as follows:

$$F_{MSL}(x) = \prod_{u=1}^{n} \left(1 - \exp\left(\frac{-x^2}{2\sigma_u^2}\right)\right)^2,$$
$$\sigma_u^2 = \frac{\left(\sin(Pu)\right)^2}{2L(Pu)^2}, \tag{3}$$

In (3), n is the number of side lobes investigated that lie to the right or to the left of the center of the sinc function. Since the sinc function is symmetric with respect to its center, the CDF for each Rayleigh distribution is squared in (3).

For a single target, the peak value (corresponding to the target location) can be expressed as $\left|\frac{1}{L}\sum_{i=1}^{L} \exp(-\jmath\frac{4\pi}{c} d\Delta f_i)\right|$, where $\Delta f_i \sim \mathcal{N}(0, \sigma^2)$ models the uncertainty of the center frequencies for the individual chirps with a standard deviation of σ. Using small-angle approximation (argument of complex exponential is small; valid if center frequency standard deviation is not too large), and Taylor expansion of the cosine term up to the second order, we can approximate the peak distribution with the Gaussian distribution having the mean of $\mathbb{E}\left[1 - \frac{8\pi^2}{c^2} d^2(\Delta f_i)^2\right]$ and the variance of $\mathrm{Var}\left[1 - \frac{8\pi^2}{c^2} d^2(\Delta f_i)^2\right]/L$. Here, $\mathbb{E}[\cdot]$ denotes the expectation.

If there are multiple targets, the tails of the sinc functions (representing each target) will interfere with the peaks at different locations. This can be thought of as a constant phasor (the peak) added with $N(L-1)$ random phasors where N is the number of targets. This can be estimated with a Rician distribution [45]. The CDF for the two different scenarios (single target

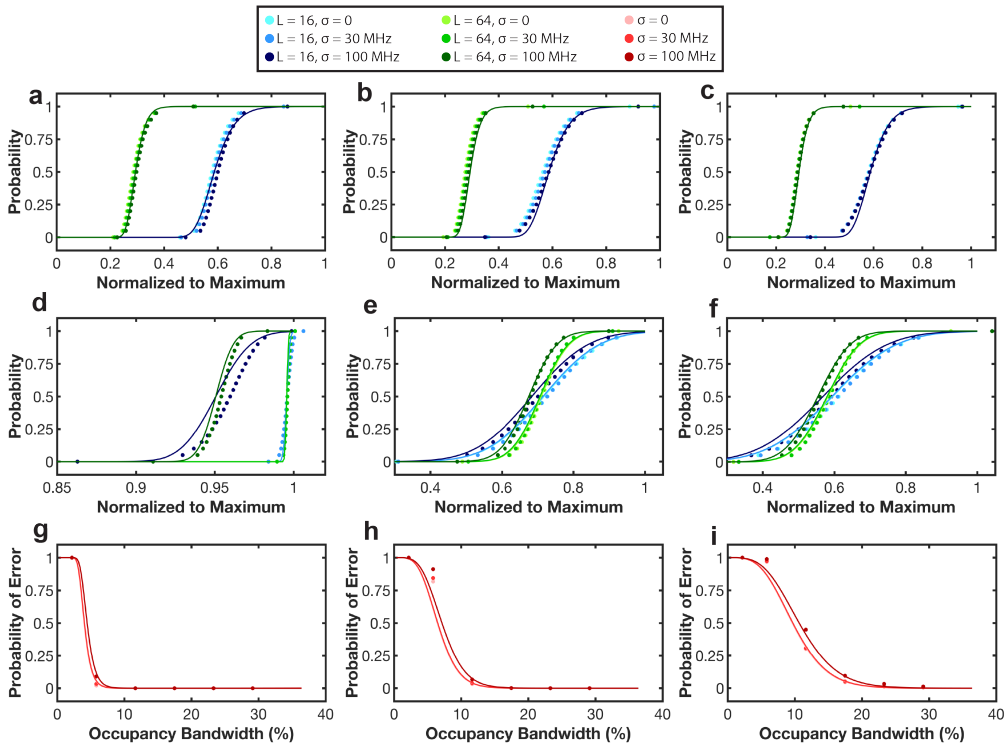

Fig. 2. Theoretical derivations and Monte-Carlo simulation results. For all demonstrated plots, single chirp bandwidth is 15 GHz, with total spanned bandwidth of 4.12 THz. Dots on the plots show simulated results with 10,000 averages, and the lines show theoretical predictions using (3), (4), and (5). **(a)** Maximum side lobe CDF for single target. **(b)** Maximum side lobe CDF for two targets. **(c)** Maximum side lobe CDF for three targets. **(d)** Peak CDF for single target. **(e)** Peak CDF for two targets of equal reflectivity. **(f)** Peak CDF for three targets of equal reflectivity. **(g)** Probability of error for 3 dB based peak detection scheme assuming single target. **(h)** Probability of error for 3 dB based peak detection scheme assuming two targets of equal reflectivity. **(i)** Probability of error for 3 dB based peak detection scheme assuming three targets of equal reflectivity.

and multiple targets) is shown in

$$F_{\text{peak}}(x) = \begin{cases} \frac{1}{2}\left[1 + \text{erf}\left(\frac{(x-1+\frac{8\pi^2}{c^2}d^2\sigma^2)c^2\sqrt{L}}{16\pi^2 d^2\sigma^2}\right)\right], & \text{if } N = 1, \\ 1 - Q_M\left(\frac{\left(1-\frac{8\pi^2}{c^2}d^2\sigma^2\right)\sqrt{2L}}{\sqrt{N-1}}, \frac{x\sqrt{2LN}}{\sqrt{N-1}}\right), & \text{otherwise,} \end{cases} \tag{4}$$

where erf represents the error function and Q_M represents the Marcum Q-function.

Assuming that the peak(s) and maximum side lobe distributions are independent, and thresholding value of a is used for detection (anything below the peak in reconstruction divided

by a is omitted), the probability of error can be estimated as in

$$p_{\text{err}} = \begin{cases} 1 - F_{MSL}\left(\frac{1}{a}\right), & \text{if } N = 1, \sigma = 0, \\ 1 - \int_0^1 f_{\text{peak}}(x) F_{MSL}\left(\frac{x}{a}\right) \mathrm{d}x, & \text{if } N = 1, \sigma \neq 0, \\ 1 - \int_0^1 f_{MSL}(x)\left(1 - F_{\text{peak}}(ax)\right) \mathrm{d}x, & \text{otherwise,} \end{cases} \tag{5}$$

where $f_{\text{peak}}(x)$ is the probability density function (PDF) for the peak(s), and $f_{MSL}(x)$ is the PDF for the maximum side lobe.

3. Monte-Carlo simulation

The accuracy of the findings within the probabilistic framework is tested with Monte-Carlo simulations. The distribution of the peak(s), maximum side lobe, and error probabilities are evaluated.

In the simulation framework, we assume single or multiple targets to be placed at a distance of 7.5 cm from the imaging system, with targets spaced 100–200 μm apart from each other. The reconstruction resolution is 5 μm, and 10,000 averages are used to estimate the distributions. Each chirp has a BW of 15 GHz, the chirp rate is 7.3026×10^{16} Hz/s, the random chirps are spaced between 1577.5 nm and 1612.4 nm, the sampling rate of the detector is 400 MHz. It is assumed that the dominant noise is the side lobes (i.e., white noise is not the limiting factor).

An error does not occur in detection if the correct number of targets is estimated, and the estimated distance of the targets is within 15 μm of the true distance. 3 dB thresholding is assumed ($a = \sqrt{2}$ in (5)) for target detection, $n = 100$, and $P = 0.005$ (chosen to make Monte-Carlo simulation results and theoretical predictions match). The thresholding, a, is a parameter to be defined before detection, and its value could be adjusted if prior information about the reconstructed targets is known. In particular, a higher threshold value is preferred if the occupancy BW is high, since targets with low reflectivity can be captured while keeping the error probability low.

The Monte-Carlo simulation results plotted with the theoretical predictions is shown in Fig. 2. Fairly good agreement is seen between simulated results and theoretical predictions. However, the accuracy of the estimation deteriorates as the standard deviation on the center frequencies increases and the number of targets is increased. These observations are consistent with derivations, as the model deviates from the Monte-Carlo simulations when the occupancy BW is small, breaking CLT; the standard deviation on the center frequencies increases, breaking small-angle approximation and the Taylor expansion.

4. Experimental demonstration

Sparse chirp OCT reconstruction results are demonstrated on metallic targets. The metallic targets were placed on a 2D motorized scanning stage to perform scanning along one dimension and image the height profile of targets. A commercially available fast tunable fiber laser, based on a sampled grating distributed Bragg reflector (SG-DBR) cavity architecture, from Insight Photonics was used to realize the proposed sparse chirp imaging system. The tunable fiber laser optical power was 2 mW.

To demonstrate the accuracy of sparse chirp OCT for height profile reconstruction, a reference metallic target with dimensions of approximately 6 cm, 6 cm, and 5 cm with height steps of 5 μm, 10 μm, 50 μm, and 100 μm was used. A common-path interferometer structure was used to mitigate noise effects commonly encountered in separate path interferometers. A partially transparent collimator was used to provide the reference path 10% of the optical power, and the remaining transmitted power (90%) was used to illuminate the metallic target.

The metallic target was scanned along one dimension using the 2D motorized scanning stage with a step size of 64 μm. The imaging parameters were as follows: 400 MHz sampling rate for

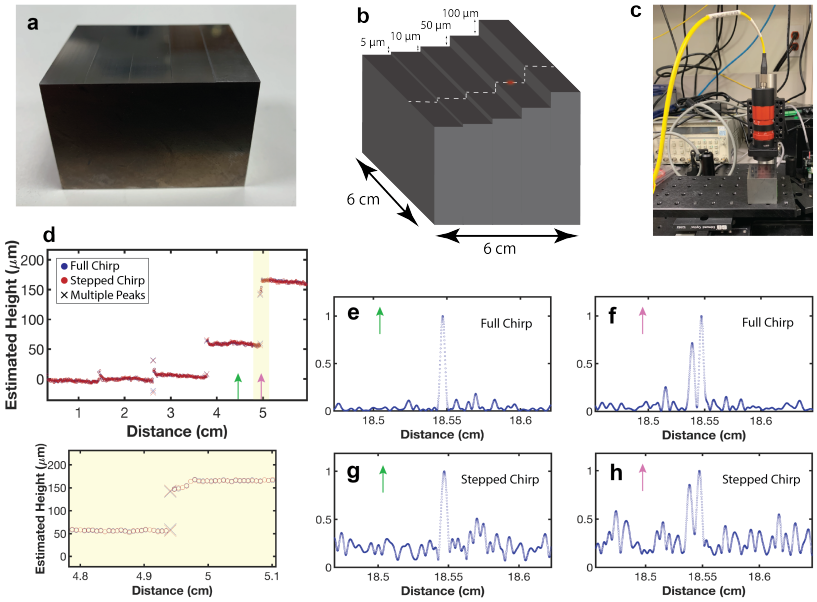

Fig. 3. Experimental test target imaging results. **(a)** Image of the test target. **(b)** 3D model for the metallic test target, with scanning direction indicated and laser beam on the path imaging the surface. **(c)** Imaging setup for resolving the surface, with the test target placed on a motorized stage for scanning and a collimator directing laser light onto the surface of the test target. **(d)** Reconstruction results using Fourier transform based processing followed by basic peak detection using 3 dB thresholding (based on max peak); crosses indicate more than one peak detected and their corresponding locations. The root mean-square error between full-chirp and stepped-chirp reconstruction is 1 μm. **(e)** Full-chirp reconstruction for the location shown with green arrow in **d**. **(f)** Full-chirp reconstruction for the location shown with pink arrow in **d**. **(g)** Stepped-chirp reconstruction for the location shown with green arrow in **d**. **(h)** Stepped-chirp reconstruction for the location shown with pink arrow in **d**.

the detector, tunable laser scanning from 1577.5 nm to 1612.4 nm, equivalent to a bandwidth of approximately 4 THz, chirp rate of 7.3026×10^{16} Hz/s, chirp bandwidth of 15 GHz (to be consistent with simulations), reconstruction resolution of 1 μm, 64 frequencies used for stepped chirp reconstruction (corresponding to roughly 23% of the total available bandwidth for the frequency sweep). According to Abbe resolution criterion, the 4 THz bandwidth should allow resolving two targets separated by more than 37.5 μm. The standoff imaging distance was approximately 18.5 cm (distance of collimator to the target), with an unambiguous imaging range of approximately 41 cm (limited by the sampling rate of the detector). The standoff imaging distance offset of 18.5 cm is removed in Fig. 3(d) to focus on the height steps.

Full-chirp reconstruction was achieved by applying FFT to the received time-domain signal. Stepped-chirp reconstruction was achieved by choosing random time intervals during the full sweep (but always choosing the beginning and the end time intervals to attain the maximum resolution, and choosing the rest of the time intervals randomly), followed by applying FFT for each time interval, and then summing the low BW chirps after appropriate phase multiplications as in (2). To make sure that the SNR for the two different reconstructions remain the same (full chirp vs. stepped chirp), different number of averages for the chirps were used. The stepped chirp approach and the full chirp approach were averaged 19 and 5 times, respectively. The measurement time for each point on the line scan was approximately 280 μs (including averaging).

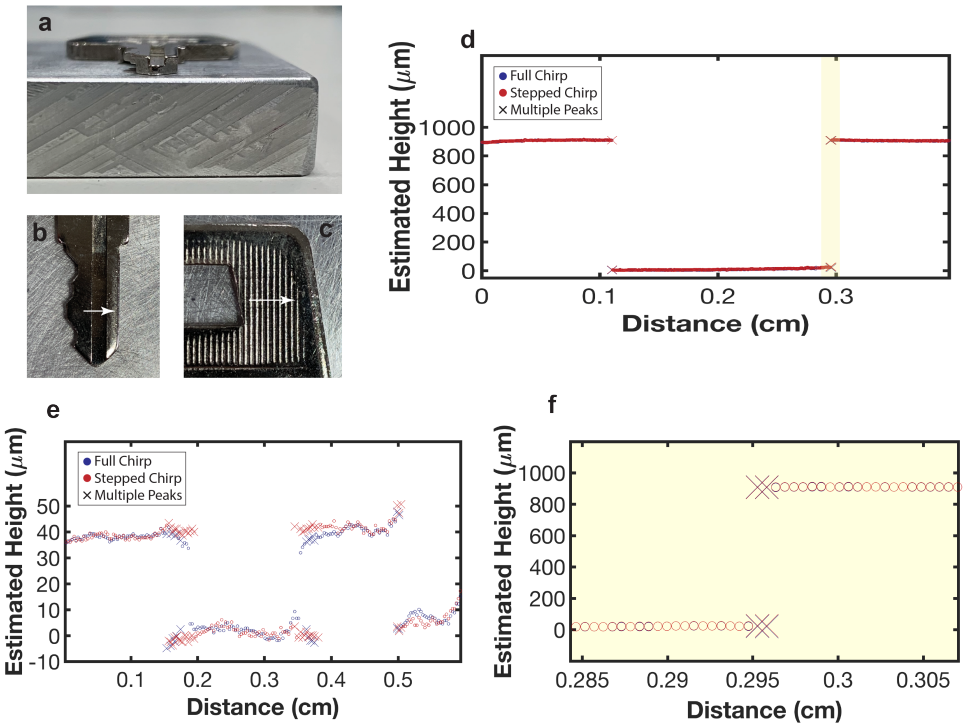

Fig. 4. Experimental imaging of a metallic key. **(a)** Side-view of metallic key. **(b)** Imaged region of key with line scan, with white arrow indicating the scanning direction for a large dip. **(c)** Imaged region of key with line scan, with white arrow indicating the scanning direction for a smaller feature area. **(d)** Reconstruction results using Fourier transform based processing followed by peak detection using 3 dB thresholding (based on max peak); crosses indicate more than one peak detected and their corresponding locations in **b**. The root mean-square error between full-chirp and stepped-chirp reconstruction is 1.3 μm. **(e)** Reconstruction results using Fourier transform based processing followed by basic peak detection using 3 dB thresholding (based on max peak); crosses indicate more than one peak detected and their corresponding locations in **c**. The root mean-square error between full-chirp and stepped-chirp reconstruction is 1.8 μm.

The camera image of the target, the 3D model, and the imaging results are shown in Fig. 3.

The reconstruction results in Fig. 3 show that stepped chirp and full chirp are both able to reconstruct the height profile, and the standard deviation between the height profile discrepancy is approximately 1 μm. In particular, the stepped chirp approach was able to resolve the imaging location where the laser beam overlapped with two surfaces with different height (step region), as shown in Fig. 3(f) and (h).

The stepped-chirp reconstruction method was also employed on imaging two different surfaces of a metallic key. To demonstrate the ability to resolve relatively small features as well as large height steps, the regions of the metallic key shown in Fig. 4(b) and (c) were imaged, where the white arrows show the scan direction by using the motorized stage. The reconstruction results for these targets are shown in Fig. 4(d) and (e).

For the large step imaging, Fig. 4(b), motorized stage stepping size of 5.33 μm was used during the line scan. The imaging parameters were as follows: 400 MHz sampling rate for the detector, tunable laser scanning from 1577.5 nm to 1612.4 nm, chirp rate of 8.398×10^{16} Hz/s, chirp

bandwidth of 15 GHz, reconstruction resolution of 1.8 μm, 64 frequencies used for stepped chirp reconstruction. Standoff imaging distance was approximately 13.8 cm (distance of collimator to the target), with an unambiguous imaging range of approximately 36 cm (limited by the sampling rate of the detector). The standoff imaging distance offset of 13.8 cm is removed in Fig. 4(d) to focus on the step region. The stepped chirp approach and the full chirp approach were averaged 18 times and 5 times, respectively. The measurement time for each point on the line scan was approximately 245 μs (including averaging). The reconstruction results in Fig. 4(d) show that stepped chirp and full chirp are both able to reconstruct the height profile, and the standard deviation between the height profile discrepancy is approximately 1.3 μm.

For imaging the smaller feature area, Fig. 4(c), motorized stage stepping size of 29.5 μm was used during the line scan. The imaging parameters were as follows: 400 MHz sampling rate for the detector, tunable laser scanning from 1577.5 nm to 1612.4 nm, chirp rate of 8.7631×10^{16} Hz/s, chirp bandwidth of 15 GHz, reconstruction resolution of 0.4 μm, 64 frequencies used for stepped chirp reconstruction. Standoff imaging distance was approximately 11.3 cm (distance of collimator to the target), with an unambiguous imaging range of approximately 34 cm (limited by the sampling rate of the detector). The standoff imaging distance offset of 11.3 cm is removed in Fig. 4(e) to focus on the smaller feature region. The stepped chirp approach and the full chirp approach were averaged 19 times and 5 times, respectively. The measurement time for each point on the line scan was approximately 235 μs (including averaging). The reconstruction results in Fig. 4(e) show that stepped chirp and full chirp are both able to reconstruct the height profile, and the standard deviation between the height profile discrepancy is approximately 1.8 μm. Assuming that full chirp can be taken as reference (since we had no actual model of the key), the stepped chirp approach is able to resolve two different height surfaces with a difference of approximately 40 μm.

Approximately 23% occupation bandwidth was selected during measurements to make sure that the probability of error is negligible. Since we know from the imaged target that we have at most two peaks within the imaged region with the optical beam, having 23% occupation bandwidth and assuming center frequency standard deviation of 100 MHz gives an error probability of approximately 0.008% according to (5). The reason behind the different chirp rates during each measurement is due to recalibration of the tunable laser before imaging the different targets.

5. Conclusions

The working principle of sparse OCT has been explained and demonstrated in this paper. The probability distributions of the peak and maximum side lobe have been derived and used for estimating the error probability of misdetection when peak based thresholding is used for image reconstruction. The accuracy of the theoretical findings was verified through Monte-Carlo simulations. These findings can serve as a simple benchmark for determining the BW occupation required for imaging certain targets, when some prior knowledge about the sparsity of the target, and the uncertainty on the center frequencies are known. Sparse OCT imaging results have been experimentally demonstrated for several different metallic surfaces. The accuracy of the reconstruction method has been first verified on a test target with prior known step heights, and then two different metallic surfaces have been reconstructed. In particular, with 23% bandwidth occupancy of 4 THz bandwidth, approximately 40 μm resolution has been demonstrated at a standoff imaging distance greater than 10 cm. The unambiguous imaging range for the experimental setup was approximately 35 cm. This range could be extended by increasing the sampling rate of the detector. The root mean-square error between full-chirp and stepped-chirp reconstruction results are approximately within 1 μm. The reconstruction accuracy could be further improved by using sparse sensing methods commonly used for sparse radar imaging. In addition, the proposed method could also be used for faster measurements of surface profile by multiplexing in the spatial domain and using sparse sensing methods (assuming the target

is spatially sparse). This would overcome having to scan through all the points on the imaged surface when spatially sparse samples are imaged, allowing significantly faster acquisition times. These results show that spectrally sparse OCT can be used for accurate mapping of targets, and if the spectral occupancy BW is chosen to accommodate the expected sparseness of the targets, sufficiently good reconstructions can be obtained. The proposed sparse OCT optical architecture could be realized using telecommunications-grade devices with a relatively simple optical architecture, therefore offering a low-cost and scalable approach for surface profiling and future applications of OCT.

6. Acknowledgement

The authors thank Dr. Hassan Mansour for useful discussions.

7. Disclosures

The authors declare no conflicts of interest.

References

1. W. Drexler, U. Morgner, F. Kärtner, C. Pitris, S. Boppart, X. Li, E. Ippen, and J. Fujimoto, "In vivo ultrahigh-resolution optical coherence tomography," Opt. Lett. **24**, 1221–1223 (1999).
2. B. Povazay, K. Bizheva, A. Unterhuber, B. Hermann, H. Sattmann, A. F. Fercher, W. Drexler, A. Apolonski, W. J. Wadsworth, J. C. Knight, P. S. J. Russell, M. Vetterlein, and E. Scherzer, "Submicrometer axial resolution optical coherence tomography," Opt. Lett. **27**, 1800–1802 (2002).
3. R. K. Ula, Y. Noguchi, and K. Iiyama, "Three-dimensional object profiling using highly accurate FMCW optical ranging system," J. Light. Technol. **37**, 3826–3833 (2019).
4. B. J. Soller, D. K. Gifford, M. S. Wolfe, and M. E. Froggatt, "High resolution optical frequency domain reflectometry for characterization of components and assemblies," Opt. Express **13**, 666–674 (2005).
5. M. Wojtkowski, R. Leitgeb, A. Kowalczyk, T. Bajraszewski, and A. F. Fercher, "In vivo human retinal imaging by Fourier domain optical coherence tomography," J. Biomed. Opt. **7**, 457–463 (2002).
6. E. A. Swanson, J. A. Izatt, M. R. Hee, D. Huang, C. Lin, J. Schuman, C. Puliafito, and J. G. Fujimoto, "In vivo retinal imaging by optical coherence tomography," Opt. Lett. **18**, 1864–1866 (1993).
7. G. J. Tearney, M. E. Brezinski, B. E. Bouma, S. A. Boppart, C. Pitris, J. F. Southern, and J. G. Fujimoto, "In vivo endoscopic optical biopsy with optical coherence tomography," Science. **276**, 2037–2039 (1997).
8. R. Dsouza, H. M. Subhash, K. Neuhaus, J. Hogan, C. Wilson, and M. Leahy, "3D nondestructive testing system with an affordable multiple reference optical-delay-based optical coherence tomography," Appl. Opt. **54**, 5634–5638 (2015).
9. B. Heise, G. Hannesschlaeger, E. Leiss-Holzinger, L. Peham, and I. Zorin, "Optical coherence tomography in nondestructive testing," in *Optics and Photonics for Advanced Dimensional Metrology,* vol. 11352 (International Society for Optics and Photonics, 2020), p. 113520Z.
10. Z. Wang, B. Potsaid, L. Chen, C. Doerr, H.-C. Lee, T. Nielson, V. Jayaraman, A. E. Cable, E. Swanson, and J. G. Fujimoto, "Cubic meter volume optical coherence tomography," Optica. **3**, 1496–1503 (2016).
11. T. Hariyama, P. A. Sandborn, M. Watanabe, and M. C. Wu, "High-accuracy range-sensing system based on FMCW using low-cost VCSEL," Opt. Express **26**, 9285–9297 (2018).
12. B. Johnson, W. Atia, S. Woo, C. Melendez, M. Kuznetsov, T. Ford, N. Kemp, J. Jabbour, E. Mallon, and P. Whitney, "Tunable 1060nm VCSEL co-packaged with pump and SOA for OCT and LiDAR," in *Optical Coherence Tomography and Coherence Domain Optical Methods in Biomedicine XXIII,* vol. 10867 (International Society for Optics and Photonics, 2019), p. 1086706.
13. D. Huang, E. A. Swanson, C. P. Lin, J. S. Schuman, W. G. Stinson, W. Chang, M. R. Hee, T. Flotte, K. Gregory, C. A. Puliafito, and J. G. Fujimoto, "Optical coherence tomography," Science **254**, 1178–1181 (1991).
14. Z. Yaqoob, J. Wu, and C. Yang, "Spectral domain optical coherence tomography: a better OCT imaging strategy," Biotechniques **39**, S6–S13 (2005).
15. M. A. Choma, K. Hsu, and J. A. Izatt, "Swept source optical coherence tomography using an all-fiber 1300-nm ring laser source," J. Biomed. Opt. **10**, 044009 (2005).
16. Y. Yasuno, V. D. Madjarova, S. Makita, M. Akiba, A. Morosawa, C. Chong, T. Sakai, K.-P. Chan, M. Itoh, and T. Yatagai, "Three-dimensional and high-speed swept-source optical coherence tomography for in vivo investigation of human anterior eye segments," Opt. Express **13**, 10652–10664 (2005).
17. V. Srinivasan, R. Huber, I. Gorczynska, J. Fujimoto, J. Jiang, P. Reisen, and A. Cable, "High-speed, high-resolution optical coherence tomography retinal imaging with a frequency-swept laser at 850 nm," Opt. Lett. **32**, 361–363 (2007).

18. M. A. Choma, M. V. Sarunic, C. Yang, and J. A. Izatt, "Sensitivity advantage of swept source and Fourier domain optical coherence tomography," Opt. Express **11**, 2183–2189 (2003).
19. M. Wojtkowski, R. Leitgeb, A. Kowalczyk, T. Bajraszewski, and A. F. Fercher, "In vivo human retinal imaging by Fourier domain optical coherence tomography," J. Biomed. Opt. **7**, 457–463 (2002).
20. R. Leitgeb, C. Hitzenberger, and A. F. Fercher, "Performance of Fourier domain vs. time domain optical coherence tomography," Opt. Express **11**, 889–894 (2003).
21. R. Huber, M. Wojtkowski, K. Taira, J. G. Fujimoto, and K. Hsu, "Amplified, frequency swept lasers for frequency domain reflectometry and OCT imaging: design and scaling principles," Opt. Express **13**, 3513–3528 (2005).
22. B. Potsaid, V. Jayaraman, J. G. Fujimoto, J. Jiang, P. J. Heim, and A. E. Cable, "MEMS tunable VCSEL light source for ultrahigh speed 60kHz-1MHz axial scan rate and long range centimeter class OCT imaging," in *Optical Coherence Tomography and Coherence Domain Optical Methods in Biomedicine XVI,* vol. 8213 (International Society for Optics and Photonics, 2012), p. 82130M.
23. D. D. John, C. B. Burgner, B. Potsaid, M. E. Robertson, B. K. Lee, W. J. Choi, A. E. Cable, J. G. Fujimoto, and V. Jayaraman, "Wideband electrically pumped 1050-nm MEMS-tunable VCSEL for ophthalmic imaging," J. Light. Technol. **33**, 3461–3468 (2015).
24. P. Qiao, K. T. Cook, K. Li, and C. J. Chang-Hasnain, "Wavelength-swept VCSELs," IEEE J. Sel. Top. Quantum Electron. **23**, 1–16 (2017).
25. M. S. Wu, E. Vail, G. Li, W. Yuen, and C. Chang-Hasnain, "Tunable micromachined vertical cavity surface emitting laser," Electron. Lett. **31**, 1671–1672 (1995).
26. R. Huber, M. Wojtkowski, and J. Fujimoto, "Fourier Domain Mode Locking (FDML): A new laser operating regime and applications for optical coherence tomography," Opt. Express **14**, 3225–3237 (2006).
27. M. Bonesi, M. Minneman, J. Ensher, B. Zabihian, H. Sattmann, P. Boschert, E. Hoover, R. Leitgeb, M. Crawford, and W. Drexler, "Akinetic all-semiconductor programmable swept-source at 1550 nm and 1310 nm with centimeters coherence length," Opt. Express **22**, 2632–2655 (2014).
28. S. Kim, M. Crose, W. J. Eldridge, B. Cox, W. J. Brown, and A. Wax, "Design and implementation of a low-cost, portable oct system," Biomed. Opt. Express **9**, 1232–1243 (2018).
29. S. Lawman and H. Liang, "High precision dynamic multi-interface profilometry with optical coherence tomography," Appl. Opt. **50**, 6039–6048 (2011).
30. D. M. Koller, G. Hannesschläger, M. Leitner, and J. Khinast, "Non-destructive analysis of tablet coatings with optical coherence tomography," Eur. J. Pharm. Sci. **44**, 142–148 (2011).
31. N. Levanon, "Stepped-frequency pulse-train radar signal," IEEE Proceedings-Radar, Sonar Navig. **149**, 297–309 (2002).
32. Y. Liu, H. Meng, G. Li, and X. Wang, "Range-velocity estimation of multiple targets in randomised stepped-frequency radar," Electron. Lett. **44**, 1032–1034 (2008).
33. M. Siddiqui, A. S. Nam, S. Tozburun, N. Lippok, C. Blatter, and B. J. Vakoc, "High-speed optical coherence tomography by circular interferometric ranging," Nat. Photonics **12**, 111–116 (2018).
34. B. Behroozpour, P. A. Sandborn, N. Quack, T. J. Seok, Y. Matsui, M. C. Wu, and B. E. Boser, "11.8 chip-scale electro-optical 3D FMCW lidar with 8μm ranging precision," in *2016 IEEE International Solid-State Circuits Conference (ISSCC),* (IEEE, 2016), pp. 214–216.
35. F. Aflatouni, B. Abiri, A. Rekhi, and A. Hajimiri, "Nanophotonic coherent imager," Opt. Express **23**, 5117–5125 (2015).
36. S. R. Axelsson, "Analysis of random step frequency radar and comparison with experiments," IEEE Transactions on Geosci. Remote. Sens. **45**, 890–904 (2007).
37. L. Zhang, Z.-j. Qiao, M. Xing, Y. Li, and Z. Bao, "High-resolution ISAR imaging with sparse stepped-frequency waveforms," IEEE Transactions on Geosci. Remote. Sens. **49**, 4630–4651 (2011).
38. Y. Ogiso, J. Ozaki, Y. Ueda, N. Kashio, N. Kikuchi, E. Yamada, H. Tanobe, S. Kanazawa, H. Yamazaki, Y. Ohiso, T. Fujii, and M. Kohtoku, "Over 67 GHz bandwidth and 1.5 V Vπ InP-based optical IQ modulator with n-i-p-n heterostructure," J. Light. Technol. **35**, 1450–1455 (2017).
39. T.-J. Ahn and D. Y. Kim, "Analysis of nonlinear frequency sweep in high-speed tunable laser sources using a self-homodyne measurement and Hilbert transformation," Appl. Opt. **46**, 2394–2400 (2007).
40. G. Raybon, J. Cho, A. Adamiecki, P. Winzer, L. H. H. Carvalho, J. C. R. F. Oliveira, A. Konczykowska, J. Dupuy, and F. Jorge, "180-Gb/s (90-GBd QPSK) single carrier transmitter using a thin film polymer on silicon I/Q modulator," in *ECOC 2016; 42nd European Conference on Optical Communication,* (2016), pp. 1–3.
41. L. R. Varshney and D. Thomas, "Sidelobe reduction for matched filter range processing," in *Proceedings of the 2003 IEEE Radar Conference (Cat. No. 03CH37474),* (IEEE, 2003), pp. 446–451.
42. J. Yang, T. Jin, C. Xiao, and X. Huang, "Compressed sensing radar imaging: fundamentals, challenges, and advances," Sensors. **19**, 3100 (2019).
43. M. Young, E. Lebed, Y. Jian, P. J. Mackenzie, M. F. Beg, and M. V. Sarunic, "Real-time high-speed volumetric imaging using compressive sampling optical coherence tomography," Biomed. Opt. Express **2**, 2690–2697 (2011).
44. D. Xu, Y. Huang, and J. U. Kang, "Volumetric (3d) compressive sensing spectral domain optical coherence tomography," Biomed. Opt. Express **5**, 3921–3934 (2014).
45. J. W. Goodman, *Statistical Optics* (John Wiley & Sons, 2015), pp. 42–51.